

# Recovering 3D tumor locations from 2D bioluminescence images

Xiaolei Huang<sup>1</sup>, Dimitris Metaxas<sup>1</sup>, Lata G. Menon<sup>2</sup>, Philipp Mayer-Kuckuk<sup>2</sup>, Joseph R. Bertino<sup>2</sup>, and Debabrata Banerjee<sup>2</sup>

<sup>1</sup> Center for Computational Biomedicine Imaging and Modeling,  
Division of Computer and Information Sciences, Rutgers University, NJ, USA

<sup>2</sup> Cancer Institute of New Jersey,  
Robert Wood Johnson Medical School, UMDNJ NJ, USA

**Abstract.** In this paper, we introduce a novel and efficient algorithm for reconstructing the 3D locations of tumor sites from a set of 2D bioluminescence images which are taken by a same camera but after continually rotating the object by a small angle. Our approach requires a much simpler set up than those using multiple cameras, and the algorithmic steps in our framework are efficient and robust enough to facilitate its use in analyzing the repeated imaging of a same animal transplanted with gene marked cells. In order to visualize in 3D the structure of the tumor, we also co-register the BLI-reconstructed crude structure with detailed anatomical structure extracted from high-resolution microCT on a single platform. We present our method using both phantom studies and real studies on small animals.

## 1. Introduction

Bioluminescence imaging (BLI) is an emerging technique for sensitive and noninvasive imaging, which can be used for monitoring molecular events in intact living animals. Important applications of this imaging technique include gene therapy and cell trafficking studies. Unlike fluorescence optical imaging approaches which require an external source of light for excitation of fluorophores, BLI generates a two-dimensional (2D) view of gene expression using a CCD camera based on the internal light produced by luciferases, catalysts in a light generating reaction, through the oxidation of an enzyme-specific substrate (luciferin) [8, 5].

The increasing use of BLI as the choice of small-animal imaging modality is based on the need for repeated imaging of the same animal transplanted with gene marked cells, which is possible using BLI. Other imaging modalities such as mPET, MRI are unsuitable for repeated imaging in a laboratory setting and require sophisticated equipment or allowance for isotope decay to image repeatedly. A complementary imaging modality to BLI is the microCT imaging, which can be used in one session to provide the high-resolution anatomical images.

The problem we tackle in this paper is to recover 3D tumor locations from 2D bioluminescence images, then register and visualize the reconstructed tumor with detailed animal geometry extracted from microCT anatomical images.

There is a need for 3D reconstruction because 2D BLI images do not provide any information on the response location in the z-axis (i.e. depth). Recently there

has been research work on bioluminescence tomography (BLT) which aims to extract the depth information [4, 11, 12]. However, as shown in [12], this inverse reconstruction problem is ill-posed and in the general case the BLT does not have a unique solution. Furthermore, real systems that implement BLT can be time consuming, and it is not easy to reconstruct the 3D images with high resolution. One potential approach suggested in [11] is to use multiple CCD cameras for simultaneous measurement of bioluminescence signals.

In this paper, we propose a novel and efficient approach to reconstruct 3D tumor locations in small animals using a series of BLI images taken by a same camera but after continually rotating the animal by a small angle. Our image-based reconstruction technique is rooted in the stereoscopy algorithm in computer vision [1]. Instead of using multiple cameras however, our experimental set-up uses a single CCD camera that is readily available in commercial BLI imaging systems (e.g. IVIS 200 imaging station) to acquire images of an animal at every rotation stage for multiple rotations clockwise from a fixed (e.g. the vertical) axis. The rotation angle is small between consecutive acquisitions to ensure the availability of good corresponding points to be used in stereo-like reconstruction. This set-up is simpler and more flexible than using multiple cameras since we can acquire any number of images by adjusting the rotation angle. Our results on both phantom study and small animals show very good reconstruction accuracy.

Registering and visualizing the reconstructed tumor structure from BLI together with detailed animal geometry extracted from microCT allows one to import multiple images on a single platform and obtain better structural and functional information. There has been extensive research on multi-modal image registration in the literature, either based on matching geometric features [9, 2] or by optimizing intensity-based energy functions [3, 10]. However, we know of no existing registration algorithms for registering the optical BLI and structural microCT. In this paper, we develop such a registration algorithm based on BLI reconstruction and structure (shape) registration. Using the registration algorithm we can locate the tumor sites relative to animal anatomical landmarks, and this knowledge will allow us to develop methods to generate MSCs with robust and improved tumor targeting capabilities in the future.

The remainder of the paper is organized as follows. We first introduce our experimental set up and data acquisition method in section 2. We introduce the algorithmic steps in 3D BLI reconstruction using a phantom study example in section 3. Then experimental results using a real animal model is presented in section 4. We conclude with discussion in section 5.

## 2. Data Acquisition

The bioluminescence images were acquired following injection of D-luciferin (given i.p. at 150mg/ml) and image reconstruction was carried out using manufacturer's (the IVIS 100 machine, by Xenogen, Alameda, CA) software. Images were acquired in a standard mode with 2x2 binning. In order to get specificity of the response in the z-axis, we design the following experimental set up. The animal to be imaged is inserted into a cylindrical 50 ml tube cut at both ends



**Fig. 1.** Examples of bioluminescence images acquired from a small animal with tumor cells growing in the abdomen.

that can be rotated by a small angle ( 12 degrees) at a time from the vertical axis. Images are acquired at every rotation stage clockwise from the vertical axis. This generates a series of images including the one without any rotation. In section 3, we will show experiments using generated phantom images rotating 11.25 degrees clockwise using luciferase positive cell lysates embedded in agarose in a 50 ml tube and collected over 20 minutes following addition of D-luciferin. For small animals such as mice (see section 4), a 50 ml tube cut at both ends and the bottom can be used as a holder. The anesthetized animal fits easily in the tube and can be placed in the imaging device without any discomfort. The animal can be rotated similar to the phantom well images and 36 rotational images can be acquired. An added advantage of the 50 ml tube is that it can be fitted with a soft foam to make the animal fit snugly in the tube and the outside of the tube can be marked with fiducial markers for anatomical reference. Fig. 1 shows some example images, between which there are small rotations. The intensity representation denotes the level of response in different locations. The bright reflections due to the tube surface are eliminated using a pre-processing filtering step before applying our reconstruction algorithm. Using this set up, we have designed computational algorithms to estimate the 3D locations of the maximum responses in BLI, which correspond to tumor center locations. We can also further extend the method to register the center of mass of several more areas near the maximum response, where the intensity is 5-10% lower from this maximum. The 3D reconstruction of these points will give an estimate of the tumor enclosing volume.

### 3. Tumor reconstruction from 2D BLI images

In this section, we introduce the algorithmic steps in 3D reconstruction from 2D bioluminescence images using images from a phantom study. In this study, lysates from cells transduced with mammalian expression vector containing luciferase is embedded in agarose plugs and incubated with the substrate D-luciferin inside a tube containing 1% agarose in Tris Acetate EDTA buffer pH 7.5. Fig. 2(1) displays a series of bioluminescence images of the tube after small rotations. The rotation angle between two consecutive images is 11.25 degrees.

The method we use to recover 3D tumor depth is based on the 3D reconstruction algorithms from computer vision using stereoscopy [1, 7]. Instead of setting up an image-capturing system with multiple cameras however, we rotate the object (tube or small animal) and take a bioluminescence picture each time the object is rotated by a small angle. Having taken a series of images with small rotation angles, we apply the following algorithmic steps to recover the geometry of the object as well as the relative depth of the tumor site.

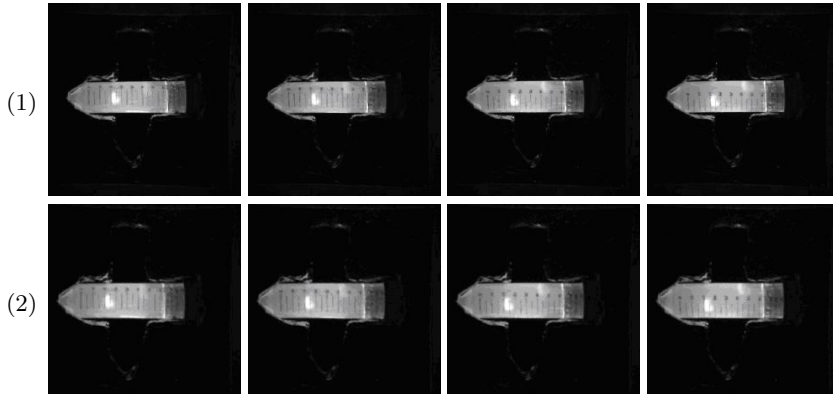


**Fig. 2.** (1) Examples from a series of bioluminescence images of a tube in the phantom study. The rotation angle between two consecutive images is 11.25 degrees. (2) Examples of images after alignment.

### 3.1. Registering images according to rotating axis

Due to noise and jittering of the image-capturing system during the rotation of the tube or small animal, the set of bioluminescence images may not be perfectly aligned. In the first step of processing, we apply an image-based method to register the set of images such that projections of the rotating axis on all images overlap in the image space. For this purpose, we define an image dissimilarity objective function based on mutual information [6, 10], and recover the translation and rotation parameters by minimizing the objective function. Suppose a source image is  $f$ , and its adjacent target image is  $g$ . In the most general case, let us consider a sample domain  $\Omega$  in the image domain of the source image  $f$ , we aim to recover the parameters  $\Theta = (T_x, T_y, \theta)$  of a global transformation  $A$  such that the mutual information between  $f_\Omega = f(\Omega)$  and  $g_\Omega^A = g(A(\Theta; \Omega))$  is maximized. Here the parameters  $T_x$  and  $T_y$  are translation parameters in the  $x$  and  $y$  directions respectively, and  $\theta$  denotes the rotation angle. And the definition for such mutual information is:

$$MI(X^{f_\Omega}, X^{g_\Omega^A}) = \mathcal{H}[X^{f_\Omega}] + \mathcal{H}[X^{g_\Omega^A}] - \mathcal{H}[X^{f_\Omega, g_\Omega^A}] \quad (1)$$

In the above formula,  $X$  denotes the intensity random variable and  $\mathcal{H}$  represents the differential entropy. Then we define the image dissimilarity objective function as:

$$E(A(\Theta)) = -MI(X^{f_\Omega}, X^{g_\Omega^A}) \quad (2)$$

Hence by minimizing this objective function  $E$ , we achieve maximizing mutual information. The calculus of variations with a gradient descent method is then used to minimize  $E$  and recover the transformation parameters  $T_x, T_y$  and  $\theta$ .

Fig. 2(2) shows the registered images. Note that small displacements and rotations between consecutive images are corrected.

### 3.2. Finding feature correspondences between consecutive images

After all images are aligned so that the projections of the rotating axes overlap, we compute feature correspondences between consecutive images in order to re-

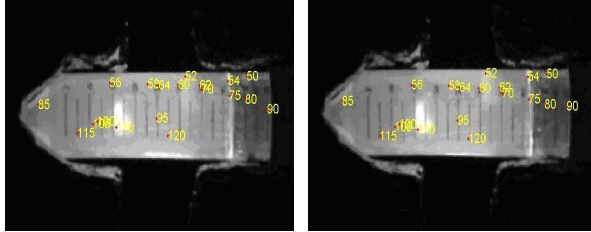


**Fig. 3.** Feature correspondences established between two consecutive images.

construct the 3D locations of those features. This is achieved by detecting corner features on both images, and establishing correspondences based on maximizing mutual information between small-neighborhood regions around the features.

To detect corner features on an image  $I$ , we consider the spatial image gradient (i.e. first order derivatives),  $[I_x, I_y]$ . For a neighborhood  $Q$  surrounding a pixel  $p$ , we form the matrix  $\mathbf{C}$ , defined as:

$$\mathbf{C} = \begin{pmatrix} \sum I_x^2 & \sum I_x I_y \\ \sum I_x I_y & \sum I_y^2 \end{pmatrix}$$

where the sums are taken over the neighborhood  $Q$ . Then we apply principal component analysis to compute the two eigenvalues  $\lambda_1$  and  $\lambda_2$  ( $\lambda_1 \geq \lambda_2$ ) of the matrix  $\mathbf{C}$ , and choose corner features as those neighborhoods with  $\lambda_1 \geq \lambda_2 > 0$  and the smaller eigenvalue  $\lambda_2$  is larger than a threshold.

To measure the similarity between small-neighborhood regions around corresponding feature points on two consecutive images, we use the multi-modal similarity measure, Mutual Information, because nonlinear changes exist in feature appearance due to planar projection after rotation. Fig. 3 shows examples of correspondences established between two consecutive images (corresponding points are marked by the same number).

### 3.3. Reconstructing 3D structure and tumor depth

Our experimental set up using a single camera and taking multiple BLI images by rotating the object is equivalent to having multiple cameras surrounding a static object. However, our set up is much simpler and does not require calibrating multiple cameras. Since we use only one camera, an orthographic projection model is used to reconstruct the locations of 3D points that project to corresponding feature points on the series of 2D images. Fig. 4 demonstrates the multi-view set up where the planes represent the projection planes for images taken from different views.

Fig. 5 demonstrates the process of determining the 3D depth of feature points by computing the intersection of 3D rays passing perpendicularly through corresponding feature points on two consecutive images mapped onto their respective projection planes. Fig. 5(a) shows 3D locations for the tube center (the intersection of the two rays in blue) and two other points on the tube surface (the intersections of rays in green). Fig. 5(b) shows the 3D location of the tumor

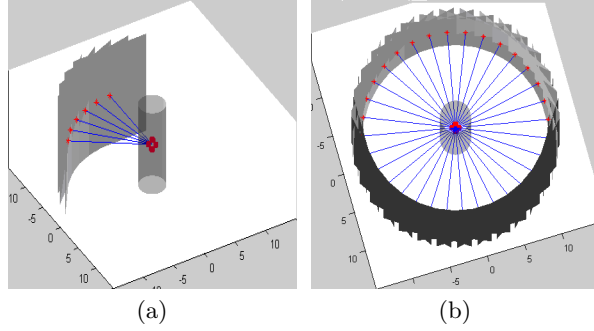


**Fig. 4.** Setting up projection plane geometry for images taken from different views. (a) some example views for consecutive images. (b) all views forming a full circle.

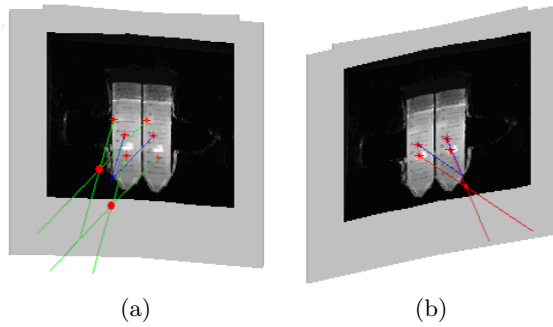


**Fig. 5.** 3D depth recovery by 3D ray intersection. (a) tube center and two feature points on the tube surface. (b) tumor center location.

center. The tumor centers on the bioluminescence images are computed as the centroid of high-intensity signal regions (drawn as asterisks on the image planes), and the intersection of 3D rays passing through tumor center locations on images taken from different views gives us the location of the tumor center in 3D.

Once we have recovered 3D points that lie on both object surfaces and the tumor, we can reconstruct the object surface, and visualize the relative location of the tumor with respect to the object surface. In the phantom study, since the object surface can be approximated using a cylinder, we determine the radius of the cylinder using the recovered 3D points on the tube surface, and render the surface as a cylinder. Fig. 6 shows our final reconstruction result for the phantom example.

Finally we establish the relationship between the reconstructed object dimension measurements in the object centered reference frame and that in the physical world. This is achieved by computing the conversion ratio based on one base measurement, such as the diameter or the length of the tube (or mouse).

In our phantom study example, validation of the reconstruction accuracy is done by comparing the recovered 3D location of the tumor center with the ground truth in our experimental set up. Visually from Fig. 6, we can see that the estimated tumor center location is within the tube, and physically we have

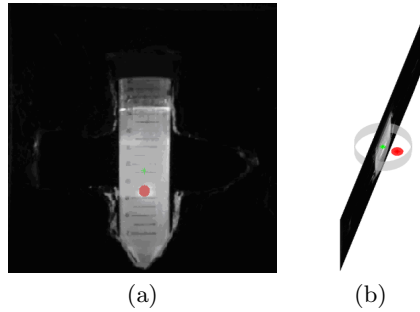


**Fig. 6.** Object surface and tumor location reconstruction result. (a) reconstructed 3D tube (gray surface) and tumor center (red sphere) superimposed on a projected bioluminescence image. (b) Another view of the reconstruction result.

measured that the distance in 3D between the true luciferase-positive cell lysates center and the recovered center is within  $2mm$ .

#### 4. Reconstruction from BLI and co-registration with microCT – on small animals

Using the algorithm described above, we can recover the tumor locations in animals. One key difference is that, because the geometry of an animal is much more complicated than a tube, it is difficult to reconstruct the 3D animal surface satisfactorily using the sparse surface points recovered. Our solution is to co-register the crude structure reconstructed from bioluminescence images with structural microCT tomographic images. This co-registration of BLI and microCT on a single platform has the advantage of combining the strengths of BLI which are: low cost and repetitive imaging, and that of microCT which are: high-resolution and containing detailed structural information.

In preparation for the BLI/microCT images, an animal was injected with  $2 \times 10^4$  tumor cells expressing luciferase. Tumors were formed in the abdomen and could be imaged by BLI (on day 12 after injection) following injection of 150mg/kg D-luciferin given intraperitoneally. The animal was anesthetized with isoflurane inhalation, injected with 150mg/kg D-luciferin and immobilized in an open 50 ml tube and placed on the imaging stage of the IVIS 100 machine (Xenogen, Alameda, CA). Images were acquired for two rotations on each side of the fixed central axis at 22.5 degrees. Examples of BLI images acquired can be seen in Fig. 1. The same animal was carried over to the microCT machine in the same position while remaining under isoflurane anesthesia. MicroCT images (512 slices) were acquired on an IMTEK microCT machine. Examples of microCT slices for the same animal are shown in Fig. 7.

We followed similar procedures to that in the phantom study for reconstruction using BLI images. First, the five BLI images are registered by aligning the projections of the rotating axes. Then both 3D mouse surface points and 3D tumor center locations are recovered in the virtual rotating camera set up using the set of bioluminescence images. Fig. 8(a-b) shows the reconstructed tumor

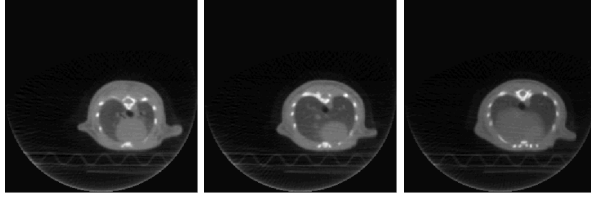


**Fig. 7.** Examples of microCT images from the same animal as in Fig. 1.

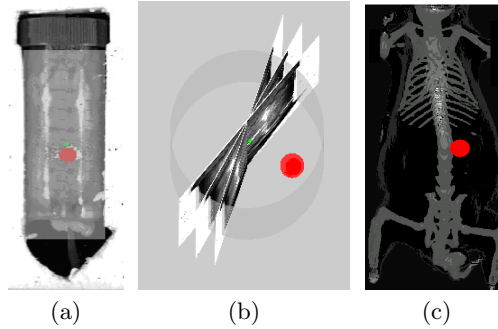


**Fig. 8.** (a) Frontal view of reconstructed tumor location superimposed on a projected image. (b) another view of the reconstructed tumor location, showing relative position with respect to three projected images. (c) reconstructed tumor superimposed on the detailed mouse geometry from microCT.

location. In our experiments, the living mouse is undergoing repetitive imaging, which allows us to obtain temporal information.

On the other hand, the mouse is imaged once in the beginning of the study. We extract the mouse surface and skeleton structures using standard segmentation and visualization techniques. We use both landmark feature information and the Iterative Closest Point (ICP) technique [13] to register the crude 3D structure reconstructed from BLI images with the detailed 3D structure reconstructed from microCT. After the registration, we are able to visualize the recovered 3D tumor location from BLI together with the detailed geometry from microCT. Fig. 8(c) shows the final registration and tumor localization result in 3D.

## 5. Discussions and Conclusions

We have presented a novel image-based framework for 3D tumor reconstruction from a series of 2D bioluminescence images and for registering reconstructed BLI structure with animal geometry extracted from high-resolution microCT images. This is the first image-based BLI reconstruction method presented, to the best of our knowledge, and the simplicity and efficiency of our framework gives it great potential in studying cell trafficking, tumor growth, response to therapy in vivo as well as imaging and analyzing processes such as hematological reconstitution following bone marrow transplantation, among others.



## References

1. N. Ayache. *Artificial Vision for Mobile Robots: Stereo vision and Multisensory Perception*. MIT Press, Cambridge (MA), 1991.
2. A. Can, C.V. Stewart, B. Roysam, and H.L. Tanenbaum. A feature-based, robust, hierarchical algorithm for registering pairs of images of the curved human retina. *IEEE Transactions on Pattern Analysis and Machine Intelligence*, 24(3):347–364, 2002.
3. A. Collignon, F. Maes, D. Vandermeulen, P. Suetens, and G. Marchal. Automated multimodality image registration using information theory. In *Proc. of Information Processing in Medical Imaging*, pages 263–274, 1995.
4. X. Gu, Q. Zhang, L. Larcom, and H. Jiang. Three-dimensional bioluminescence tomography with model-based reconstruction. *Optics Express*, 12(17):3996–4000, 2004.
5. B. Iris, Y. Zilberman, E. Zeira, E. Galun, A. Honigman, G. Turgeman, T. Clemens, Gazit Z., and Gazit D. Molecular imaging of the skeleton: quantitative real-time bioluminescence monitoring gene expression in bone repair and development. *J. Bone Miner. Res.*, 18:570–578, 2003.
6. F. Maes, A. Collignon, D. Vandermeulen, G. Marchal, and P. Suetens. Multimodality image registration by maximization of mutual information. *IEEE Transactions on Medical Imaging*, 16(2):187–198, 1997.
7. D. Marr and T. Poggio. A computational theory of human stereo vision. *Proc. R. Soc. Lond. B*, 204:301–328, 1979.
8. P. Mayer-Kuckuk, L. G. Menon, R. G. Blasberg, J. R. Bertino, and D. Banerjee. Role of reporter gene imaging in molecular and cellular biology. *Biol. Chem.*, 385:353–361, 2004.
9. J.-P. Thirion. New feature points based on geometric invariants for 3D image registration. *International Journal of Computer Vision*, 18(2):121–137, May 1996.
10. P. Viola and W. Wells. Alignment by Maximization of Mutual Information. In *Proc. of IEEE International Conf. on Computer Vision*, pages 16–23, 1995.
11. G. Wang, E. A. Hoffman, G. McLennan, L.V. Wang, M. Suter, J. F. Meinel, and et al. Development of the first bioluminescent ct scanner. *Radiology*, 229(P):566, 2003.
12. G. Wang, Y. Li, and M. Jiang. Uniqueness theorems in bioluminescence tomography. *Med. Phys.*, 31:2289–2299, 2004.
13. Z. Zhang. Iterative point matching for registration of free-form curves and surfaces. *International Journal of Computer Vision*, 13(2):119–152, 1994.